Design of membraneless gas-evolving flow-through porous electrodes

Rajaei, H.; Rajora, A.; Haverkort, J. W.

DOI
10.1016/j.jpowsour.2020.229364

Publication date
2021

Document Version
Final published version

Published in
Journal of Power Sources

Journal of Power Sources 491 (2021) 229364

Contents lists available at ScienceDirect

Journal of Power Sources

journal homepage: www.elsevier.com/locate/jpowsour

Design of membraneless gas-evolving flow-through porous electrodes

H. Rajaei, A. Rajora, J.W. Haverkort *

Process & Energy Department, Delft University of Technology, Leeghwaterstraat 39, 2628 CB, Delft, the Netherlands

HIGHLIGHTS

- Membraneless cells with lower resistance than cells with diaphragm are demonstrated.
- A minimum electrolyte velocity prevents gas from entering the interelectrode gap.
- An analytical multiphase porous electrode model predicts the minimum required velocity.
- Significant total energy savings are possible by using flow instead of a membrane.
- Simple expressions are provided for design parameters that minimize the energy losses.

GRAPHICAL ABSTRACT

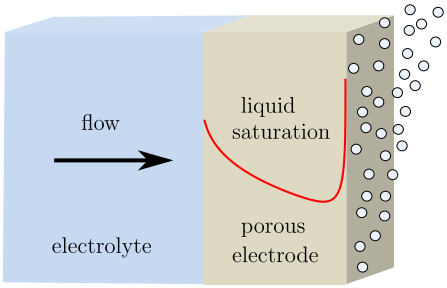

ARTICLE INFO

Keywords:
Flow-through porous electrodes
Membraneless design
Electrochemical reactor

ABSTRACT

Flow-through electrolyzers, with flow parallel to the current, are used in a wide range of industrial applications. The presence of flow avoids concentration gradients but can also be used to separate evolved gases, allowing membrane-less operation. In this work, we propose a simple multiphase flow-through electrode model. We derive and experimentally validate an analytical expression for the minimum velocity required to ensure effective gas separation. From this relation, we analytically derive design parameters that show that significant energy savings can be made using flow, compared to a physical separator.

1. Introduction

Porous flow-through electrodes have been studied for a long time due to their superior mass transfer [1,2]. Flow-through porous electrodes are traditionally used in electrosynthesis [3,4], redox flow batteries [5–7], metals removal from waste streams [8–10], electrochemical destruction of cyanide [11,12], and water electrolysis [13–17].

The flow in a porous electrode can be parallel to the current as in Fig. 1, normal, or a combination as in the interdigitated configuration [18]. A flow-through electrode with flow parallel to the current has traditionally in the literature often been referred to as flow-by electrodes [19,20]; a term nowadays, particularly in the flow battery literature, more commonly reserved for flow that largely bypasses the electrodes in a separate channel next to the electrodes, see e.g. Refs. [6,21]. Here we will consider the flow configuration of Fig. 1 in which the flow enters in between and flows out *through* the electrodes. This configuration has similarities with both cross-flow and dead-end separators used for filtration.

In many electrochemical processes, the gases are evolved in a liquid electrolyte; including the chlor-alkali process used for producing chlorine, the electrosynthesis of chlorate [22], or fluorine [23], the Hall-Héroult process for smelting aluminium, electrowinning of metals,

* Corresponding author.
E-mail address: J.W.Haverkort@tudelft.nl (J.W. Haverkort).

https://doi.org/10.1016/j.jpowsour.2020.229364
Received 21 October 2020; Accepted 15 December 2020
Available online 7 February 2021

Nomenclature

$\mathscr{E}$	Effectiveness factor, [−]
m	Exponent in effective conductivity κs^m , [−]
q	Exponent in the relative permeability s^q , [−]
s	Liquid saturation, [−]
ϵ	Porosity, [−]
η	Activation overpotential, [V]
γ	Surface tension, [N/m]
κ	Effective electrode conductivity $\approx \kappa_0 \epsilon^{1.5}$, [−]
λ	Pore size distribution index
μ	Dynamic viscosity, [Pa· s]
c_1	Material constant $K/\epsilon^3 d_{\max}^2$, [−]
$'$	Derivative d/dx
0	Subscript indicating electrode entrance $x = 0$
Δp	Total pressure drop $\Delta p_{\text{el}} + \Delta p_{\text{gap}}$, [Pa]
A	Frontal electrode area hw , [m^2]
b	Tafel slope, [V]
C	Reactant inlet concentration, [mol/m^3]
$d_{\max}$	Maximum pore diameter, [m]
F	Faraday constant 96485.3329, [C/mol]
h	Electrode/gap height, [m]
i	Local electronic current density, [A/m^2]
j	Current density magnitude, [A/m^2]
K	Electrode permeability, [m^2]
L	Electrode thickness, [m]
l	Gap width, [m]
N	Ratio $\Delta p/\Delta p_{\text{gap}}$, [Pa]
n	Electrons per reactant molecule
p	Pressure, [Pa]
P_{pump}	Power lost to friction, [W]
p_t	Threshold pressure $4\gamma/d_{\max}$, [Pa]
R	Gas constant 8.31446, [J/mol/K]
T	Temperature, [K]
u	Superficial velocity in x-direction, [m/s]
V_m	Molar volume, [m^3/mol]
w	Electrode/gap depth, [m]
x	Streamwise coordinate in electrode, [m]

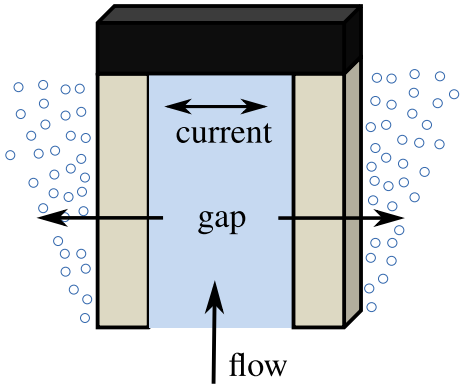

Fig. 1. A schematic view of the flow-through configuration considered with, inside the porous electrodes, flow *parallel* to the current, *outwards* from the gap, *through* the electrodes.

various forms of CO_2 reduction [24], and water electrolysis.

Typically a membrane or separator is used to avoid gases crossing-over to the opposing electrode where they may react back and cause inefficiencies, cause product impurity, or safety concerns as in the case of oxygen and hydrogen for example [25–27]. Various membraneless designs have also been proposed, for example based on selective coating [28] or lift forces on bubbles [29]. Since a membrane or separator adds costs, resistance, and potential degradation, there seems significant potential for membraneless designs. The design under consideration here uses outward flow to separate the produced gases, as depicted schematically in Fig. 1. This configuration was already studied for water electrolysis in, e.g. Refs. [13,30,31] but only recently its potential for membraneless operation has been highlighted in Refs. [14,15,32,33].

Many studies have been devoted to modelling flow-through electrodes [19,20,34,35] focusing mostly on mass transfer [31,36,37] while far fewer include the effect of gas evolution [38–42]. All these models assume that distinct bubbles move with a velocity proportional to the liquid velocity. This assumption is likely invalidated when the pores become smaller than the 100 μm [22] that is typical for the diameter of electrolytically generated bubbles. For the small pores typically present in rocks or the diffusion layers of PEM fuel cells [43–45] and electrolyzers [46–48], often the assumption is made that gas forms continuous pathways rather than bubbles [49]. This can be likened to the annular flow regime in pipe flow. In this case, Darcy's law, which supposes a linear relationship between pressure gradient and velocity, can be assumed to hold approximately. Although this is a strong simplification with various limitations [50], we will discuss here the conclusions that follow from such a model and contrast it with the hitherto used bubble flow assumption.

A largely unanswered question is: what values for the various geometrical design parameters in Fig. 1, like electrode thickness, height, gap thickness, and pore size, are optimal from the perspective of energy efficiency. The answer crucially depends on both the flow direction and the minimum required flow rate. When a flow is used for mass transfer, various useful references exist [19,20,35,51,52]. However, when a flow is used to allow membrane-less operation of a gas-evolving electrolyzer very little is known. Reference [16] achieved, in a membraneless alkaline water electrolyzer, a current density of roughly 2 A/cm^2 at a cell voltage of 2.5 V and 4 A/cm^2 at 3.3 V. Compared to, typically much thinner, separators the used 2.5 mm gap seems to leave significant room for improvement. Smaller gaps, however, also require smaller pores, to ensure good distribution of flow, hence our interest in models beyond the assumption of bubbly flow.

Recently [17,53] an extremely high current density of 25 A/cm^2 was obtained at 3.5 V, for more than 100 h, in an alkaline water electrolyzer with flow through a microfibre nickel felt *perpendicular* to the current. These results were obtained using an extremely thin polyethersulfone 0.1–0.15 μm thickness membrane, which showed immediate failure due to heat at even higher current densities.

The likely reasons that high multi-A/cm^2 current densities have been achieved in alkaline systems only in the presence of flow is likely due to flow-enhanced mass transfer of dissolved gases, electrolyte, and bubbles, reducing the Nernstian open-circuit potential or concentration polarization [54,55], bubble overpotentials [56–58] and increase the limiting current density [27,59], respectively.

Our primary goal here will be to determine the optimal geometrical and operational conditions for membrane-less flow-through electrolysis, to ascertain whether this can be competitive with conventional operation with a separator. A question that, however, first has to be answered is: what is the required flow velocity, as a function of current density, to allow membraneless operation.

The remainder of the paper is organized as follows. The proposed multiphase model to determine the minimum liquid velocity is discussed in Section 2. Experimental verification and observations with an alkaline water electrolyzer setup are discussed in Section 3. In section 4, we

determine the optimal design parameters. Finally, we summarize and discuss our main findings in Section 6.

2. Multiphase flow-through electrode model

2.1. Governing equations

In the model previously used in Refs. [38–42] and considered in Appendix A.2, gas bubbles always move in the direction of the flow so that any non-zero velocity allows effective gas separation. Obviously, especially at large current densities, gas bubbles will also enter the gap between the electrodes, unless an unknown minimum flow-through liquid velocity is used. Here we consider a simple multiphase electrode model to obtain explicit analytical expressions for this velocity. We consider pores that are small compared to the electrode thickness so that an average description over many pores can be used. The gas will be assumed to form continuous pathways so that the extended Darcy equation can be used.

For a hydrophilic electrode we may use the following differential equation, discussed in more detail in Ref. [49], to describe the liquid fraction or *saturation* s,

$$\frac{dp_t s^{-1/\lambda}}{dx} = -\frac{\mu_g u_g}{K(1-s)^q} + \frac{\mu_l u_l}{K s^q}. \tag{1}$$

The left-hand side shows the derivative of the capillary pressure, the gas pressure minus the liquid pressure, with respect to the x-coordinate through the electrode; with $x = 0$ upstream, at the gap, and $x = L$ downstream, at the rear. According to Darcy's law, the gas and liquid pressure gradients are proportional to the gas and liquid superficial velocities u_g and u_l and viscosities μ_g and μ_l. The capillary pressure $p_t s^{-1/\lambda}$ is related to the saturation through the Brooks-Corey relation, with λ the pore size distribution index - a smaller value corresponding to a more narrow distribution. The threshold pressure p_t is the capillary pressure at $s = 1$, so corresponding to the largest pore. It is routinely measured in the analytical porosimetry technique as the 'bubble point pressure', the minimum pressure that has to be applied to the gas phase on one side of a porous medium to see bubbles appearing on the other side.

The permeability K for the liquid is reduced by the presence of the gas through the 'relative permeability' s^q, and similarly $(1-s)^q$ for the gas permeability. Although actually only consistent with the Brooks-Corey relation for $q = 3$ in the limit $\lambda \to \infty$ [49,60], often a power-law fits well to experiments, see for example Ref. [61]. We note that in the following analysis, approximations near $s = 1$ are used.

Approximating the pores as cylinders with a maximum diameter $d_{\max}$ we can write

$$p_t = \frac{4\gamma}{d_{\max}}, \quad K = c_1 \epsilon^3 d_{\max}^2. \tag{2}$$

Here ϵ is the porosity and c_1 a material-dependent parameter [49,60,62,63].

If both the gas and the electronic current move to the right through the porous electrode, the gas velocity u_g will be proportional to local electronic current density i by Faraday's law as

$$u_g = \frac{V_m i}{nF}. \tag{3}$$

Here the gas molar volume of an ideal gas $V_m = RT/p$, n is the number of electrons per gas molecule, and F is Faraday's constant giving the charge of a mole of electrons.

At the gap side $x = 0$ both u_g and i vanish, and at the rear both are at their maximum and $i(x = L) = j$ is equal to the current density magnitude. In general we can write $i'_0 \equiv \frac{di}{dx}|_{x=0} = \frac{1}{\mathscr{E}} \frac{j}{L}$, in terms of the electrode effectiveness factor $\mathscr{E}$ as illustrated in Fig. 2. Using the approximation of Eq. (A.12) this gives

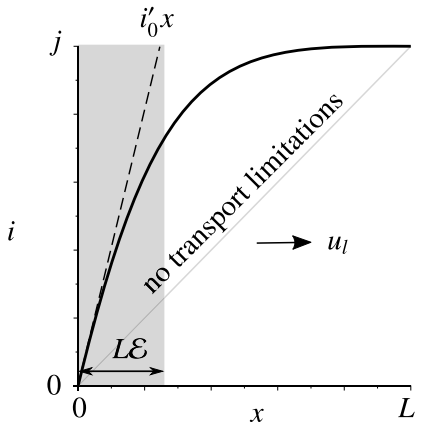

Fig. 2. A possible profile of the electronic current i throughout the electrode, with most of the current generated in the shaded region within a distance $\mathscr{E}L$ to the gap, minimizing the ohmic drop that ions have to travel.

$$i'_0 \approx \frac{j}{L}\left(1 + \frac{jL}{2\kappa b}\right), \quad \kappa \approx \epsilon^{1.5}\kappa_0. \tag{4}$$

The effective conductivity of the porous electrode is often approximated by the Bruggemans relation $\kappa \approx \epsilon^{1.5}\kappa_0$ in terms of the electrolyte conductivity κ_0. Here we neglect the influence of the gas fraction, which

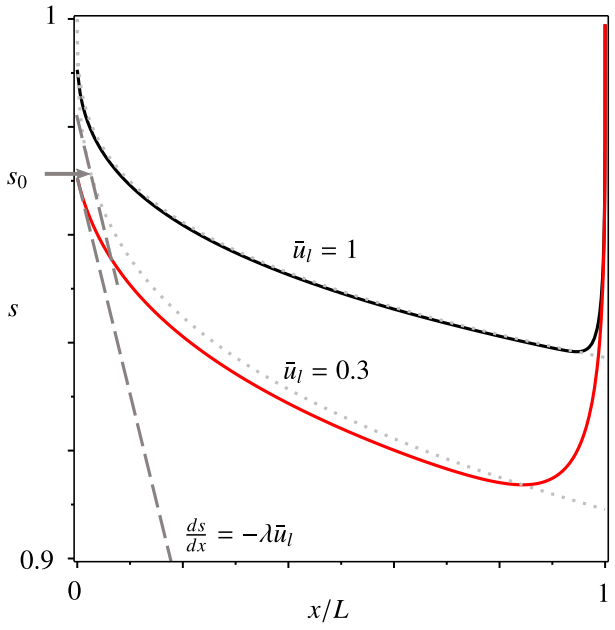

Fig. 3. The saturation profile throughout the electrode from solving Eqs. (1) and (3) with a linearly current density profile, or $\frac{ds^{-1/\lambda}}{d(x/L)} = -\frac{\bar{j}(x/L)}{(1-s)^q} + \frac{\bar{u}_l}{s^q}$ with $q = 3$, $\lambda = \frac{4}{3}$, $\bar{j} \equiv \frac{\mu_g L}{K p_t} \frac{V_m j}{nF} = 3{\cdot}10^{-4}$, and $\bar{u}_l \equiv \frac{\mu_l L u_l}{K p_t} = 1$ and 0.3. At the rear side, we somewhat arbitrarily assumed $s(L) = 0.999$ but the exact value can be seen to impact only the solution near $x = L$. As the liquid velocity is decreased, $s(x = 0)$ decreases, which could result in an accumulation of gas bubbles near the entrance. Over most of the domain the right-hand side of Eq. (1) approximately vanishes so that $s \approx 1/(1 + (\bar{j}(x/L)/\bar{u}_l))^{1/q})$, a solution that is indicated by the dotted lines. Equating the derivative of this solution to that of the solution near $x = 0$, indicated by the dashed lines, we obtain $s_0 \approx 1 - \sqrt{\bar{j}/q\lambda}/\bar{u}_l = 0.99$ and 0.97 for $\bar{u}_l = 1$ and $\bar{u}_l = 0.3$, respectively, in agreement with the numerical result. This expression for s_0 is used to derive Eq. (5).

we show in Appendix A to be modest.

2.2. Numerical solutions

Fig. 3 shows the solution to Eqs. (1) and (3) for a linearly varying current density $i = (x/L)j$ and a boundary condition $s(x = L) = 0.999$. The actual value used is not of much influence for the solution near $x = 0$. The produced gases hydrogen and oxygen are created in dissolved form first and advected with the flow, before a sufficiently high supersaturation causes nucleation of gas bubbles that grow and coalesce. We therefore assume that a minimum saturation $s(x = 0) = s_0$, which can be slightly below unity that will allow effective membrane-less operation without bubbles entering the gap. Next, we aim to find an analytical expression for the associated minimum liquid velocity.

2.3. Analytical solution

The numerical solutions reveal two distinctive features that can be used to find an analytical approximation for the required liquid velocity. First, the second term in Eq. (1), representing the frictional pressure gradient due to liquid flow, dominates near $x = 0$ when $s_0 \approx 1$. Locally, this allows the equation to be approximated by $-\frac{1}{\lambda}p_t s' = \frac{\mu_l u_l}{K}$.

A second observation from the numerical solutions of Fig. 3 is that, in the rest of the domain, the two terms in Eq. (1) approximately cancel so that $\left(\frac{1-s}{s}\right)^q \approx \frac{\mu_g u_g}{\mu_l u_l}$. Taking the derivative of this expression at $x = 0$ gives $-q(1-s_0)^{q-1}s_0^{-q-1}s' \approx \frac{\mu_g u_{g0}'}{\mu_l u_l}$, where $u_{g0}' \equiv \frac{du_g}{dx}|_{x=0}$. Matching the two foregoing approximations for s' gives $u_l^2(1-s_0)^{q-1}s_0^{-q-1} = \mu_g K p_t u_{g0}'/q\lambda\mu_l^2$. This solution for s_0 was compared with the numerical result and found to give excellent agreement as long as $s_0 \gtrsim 0.9$. From Eqs. (3) and (4) $u_{g0}' = \frac{V_m}{nF}\frac{j}{L}\left(1+\frac{jL}{2\kappa b}\right)$ so that with Eq. (2) we obtain

$$u_l = \sqrt{\frac{c_2 j d_{\max}}{L}\left(1+\frac{jL}{2\kappa b}\right)}, \tag{5}$$

with $c_2 = \frac{4\gamma c_1 \epsilon^3 s_0^{q+1}}{q\lambda(1-s_0)^{q-1}}\frac{\mu_g}{\mu_l^2}\frac{V_m}{nF}$ [m^4/C/s]. If we assume that the minimum saturation s_0 required to avoid bubbles in the gap is approximately constant, Eq. (5) gives an expression for the minimally required liquid velocity. This velocity is predicted to increase with $\sqrt{j/L}$ or j for electrodes that are thin or thick relative to $\kappa b/j$, respectively. The associated value of s_0 in this model is a constant that has to be obtained from experiments.

3. Experiments

3.1. Materials and methods

To validate the above model predictions we consider a typical "filter press"-like [64,65] zero-gap [66] alkaline water electrolyzer setup, consisting of a stacking of several transparent perspex plates, see Fig. 4. A 30%w aqueous KOH electrolyte (from Honeywell Fluka with 85% purity) is pumped through the set-up using a Heidolph peristaltic pump at ambient conditions, and back through an ultrasonic cleaner to degas [67]. A BK Precision 9151 power source is used to supply current and measure the cell voltage.

We use two different fibrous nickel electrodes shown in Fig. 4, one felt and one plain weave mesh, and also two different plain weave nylon meshes as spacers. The geometrical features of these materials are summarized in Table 1.

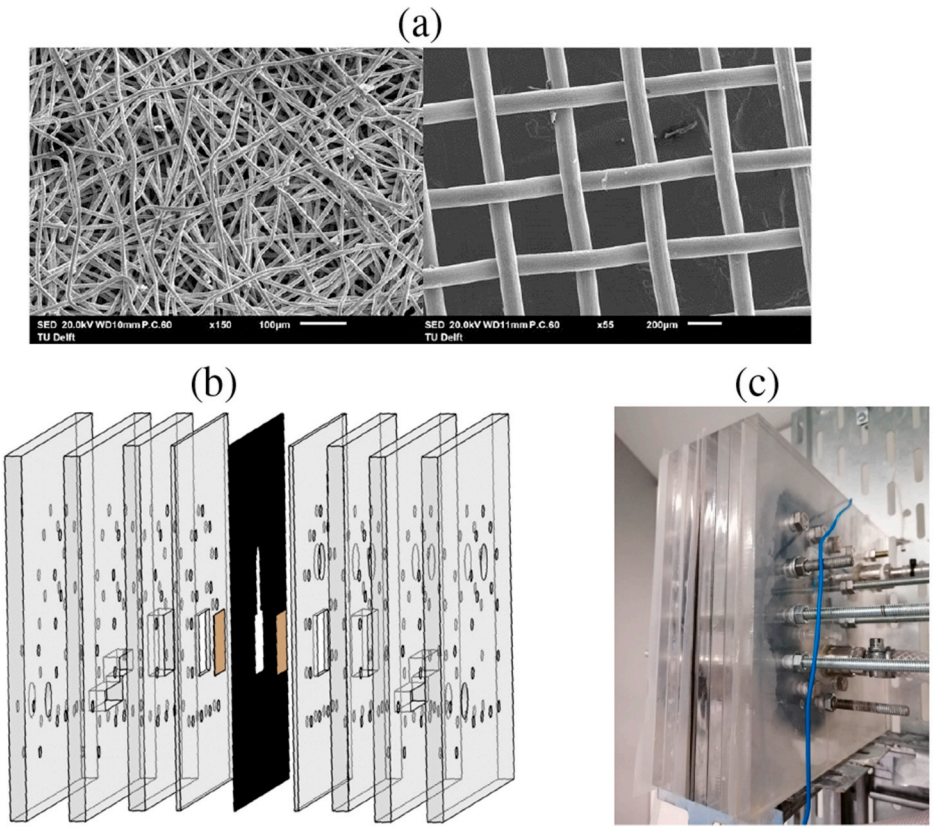

Fig. 4. Top: Images of electrode morphologies using a Scanning Electron Microscope (SEM). (a) The SEM image on the left is the nickel felt electrodes with a 'filter size' of $d_{\max} = 8$ µm and the image on the right is the mesh electrodes with an aperture of $d_{\max} = 300$ µm. (b) An exploded view of various PMMA layers (grey), electrodes (brown rectangles), and the rubber gasket (black) and (c) showing the various compression bolts, electrolyte inlet (top right) and outlet (bottom right). (For interpretation of the references to colour in this figure legend, the reader is referred to the Web version of this article.)

The first plain-weave nylon mesh consists of fibres of a specified 31 μm diameter giving, with some compression of the fibres, a reported thickness 53 μm. These are pressed to the electrodes in configuration 1 of Fig. 5 by the flow and on the circumference by a rubber gasket, see Fig. 4. The second, much coarser, mesh of Table 1 is used as a spacer to fill the entire gap, in configuration 2 of Fig. 5.

3.2. Pressure drop

An estimate of the pressure drop Δp_{el} through the Ni-felt electrodes was obtained using the reported pump curve, a magnetically driven pump (HTP-B, March May Ltd.). Correcting for an estimate of pressure drop in the tubes, we found a pressure drop through the electrodes $\Delta p_{el} \approx 0.2$ bar at a superficial electrolyte velocity $u_l = 4.25$ mm/s. As shown in Appendix A.3 we can neglect the effect of the produced gas on the pressure drop, so that $\frac{\Delta p_{el}}{L} \approx \frac{\mu_l u_l}{K}$. This gives $K \approx 1.3{\cdot}10^{-13}$ m^2. Using this in Eq. (2), with $\epsilon = 0.75$ and $d_{max} = 8$ μm gives $c_1 \approx 5{\cdot}\ 10^{-3}$.

3.3. Cell voltage

Fig. 7 shows the recorded time-average (≈ 200 s) steady-state (after ≈ 40 s) cell voltage for configuration 1 of Fig. 5 with the Ni-felt electrode, as a function of liquid flow rate, for three different current densities. The cell voltage for the largest used flow rate was subtracted. The cell voltage can still be significantly reduced by applying a catalytic coating, reducing the gap width, and using an elevated temperature to increase the electrolyte conductivity. However, here we are interested in the increase in cell potential that is observed when the velocity drops below a few mm/s. The dramatic increase of almost 1.5 V for $j = 4000$ A/m^2, shown in Fig. 7, can only be explained by an additional ohmic drop jl/κ introduced by gas entering the gap. In the presence of a nylon mesh, as in configuration 1, the additional voltage disappears again upon applying a larger flow rate showing that bubbles can be pushed into the electrodes. Approximating the electrolyte conductivity as $\kappa_0(1-\epsilon_g)^{1.5}$ [68], with $l = 1.1$ mm and $\kappa_0 \approx 60$ S/m [69], we find that a very large gas fraction $\epsilon_g \approx 0.86$ is required to explain the observed overpotential. Note that this is beyond the maximum packing of uniform spherical bubbles, requiring the gap to be almost completely filled with large gas slugs. To investigate this further, we made a dedicated visually easily accessible set-up, as detailed in the next section.

3.4. Visualization inside porous electrode

We designed and carried out an experiment to visualize what happens inside a gas-evolving porous electrode [70]. The mesh electrode of Table 1 is sandwiched horizontally between two perspex layers, see Fig. 6(a). Using a syringe pump, the electrolyte flows from right to left through the mesh electrode. Images from a camera mounted above the set-up are shown in Fig. 6(b) for two different flow rates, $Q \approx 0.5$ and ≈ 9 ml/min. With a width of 1 cm and a height of 0.3 mm, this amounts to superficial velocities of 2.8 mm/s and 50 mm/s, respectively. At the highest flow rate, primarily very small bubbles can be seen, most of which move along with the liquid flow. For the lowest flow rate, however, very large gas slugs form, both inside the electrode, and in front of the electrode. Of course, this configuration is substantially different from that studied in the previous section. The much larger pores and the

Table 1
All measures with unit length here, including the thickness L, are in μm. The 'maximum pore size' d_{max} for the nickel felt and nickel and nylon meshes represent the "filter size" and aperture widths reported by the suppliers. The fibre diameters d_f are estimated from SEM images, or reported by the supplier in case of the nylon meshes. The porosity ε of the felt is obtained from a densitometric measurement, or from geometry for the nickel mesh. For the volumetric surface area we used $a \approx 4(1-\epsilon)/d_f$.

	L	d_{max}	d_f	ϵ [−]	a_s [m^{-1}]
Ni-felt	300	8	10	0.75	10^5
Ni-mesh	300	300	120	0.6	$1.3{\cdot}10^4$
Nylon 1	53	35	31	–	–
Nylon 2	1100	1930	550	–	–

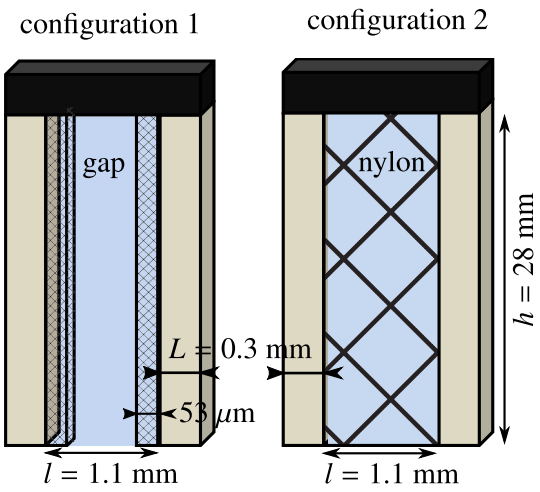

Fig. 5. In Configuration 1, nylon meshes of thickness 53 μm, aperture d_{max} = 35μm, and dimensions slightly larger than the electrodes, are pressed to the electrodes at their circumference by a 1 mm thick rubber gasket. In Configuration 2, a nylon mesh of thickness 1.1 mm and aperture $d_{max} = 1.93$ mm is used as a spacer between the electrodes.

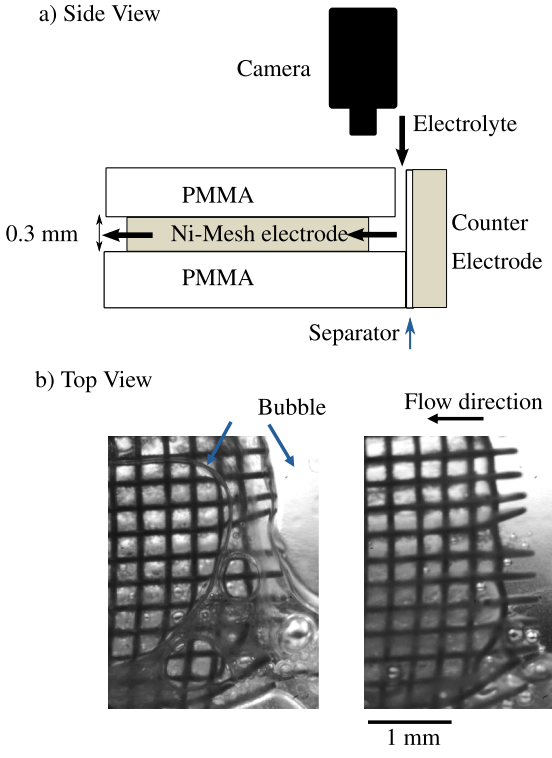

Fig. 6. a) A schematic side-view of the visualization setup in which electrolyte flows from right to left through the mesh electrode while a camera records from the top b) Top-view images of a slug flow regime at an electrolyte velocity $u_l \approx$ 3 mm/s, and a bubble flow regime at higher electrolyte flow rates of $u_l \approx$ 50 mm/s.

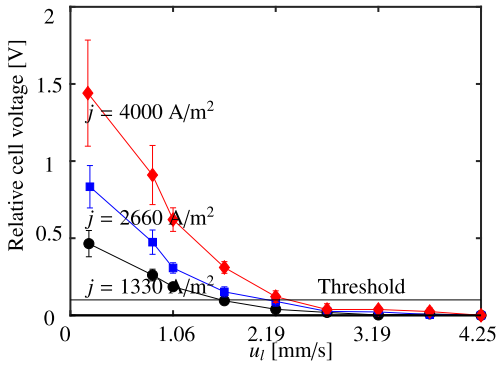

Fig. 7. The relative cell voltage measured in configuration 1 with nickel felt electrodes, as a function of the superficial liquid velocity, for three different current densities. We subtracted the cell voltage ≈ 2.4, 2.85, and 3.5 V recorded at the maximum flow rate for the three current densities, respectively. The horizontal solid line is the threshold of 100 mV used in Fig. 8.

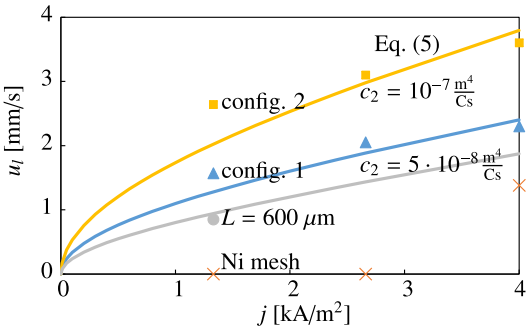

Fig. 8. The measured minimum required liquid velocity u_l to keep the bubble associated overpotential below 0.1, as outlined in Fig. 7. For configuration 1 (diamonds) we varied both the electrode thickness (circles) and the aperture size (crosses). The continuous lines show a comparison with Eq. (5) using $c_2 = 5{\cdot}10^{-8}$ m^4/(Cs). For configuration 2 (squares) a larger value $c_2 = 1{\cdot}\ 10^{-7}$ m^4/(Cs) is required to obtain a reasonable agreement, while for the Ni-mesh we do expect a bubbly flow regime in which the theory behind the equation does not hold.

presence of the perspex plates significantly influence the bubble shapes. Nevertheless, these observations show a plausible mechanism by which the measured voltage increase can be interpreted - due to large gas slugs accumulating in front of and inside the electrodes.

3.5. Model validation

To compare the cell voltage measurements of Fig. 7 with the multiphase flow-through electrode model of section 2 we somewhat arbitrarily define the minimum required liquid velocity as that which keeps the bubble-induced losses below 0.1 V, as shown in Fig. 7. The associated minimum liquid velocities are plotted in Fig. 8.

With the values from Table 2 we have $2\kappa b/L \approx 1.3$ A/cm^2 so that, in the range of current densities of Fig. 8, Eq. (5) predicts that the minimum liquid velocity scales approximately with $\sqrt{j/L}$. This proportionality is indeed approximately observed in the data of Fig. 8, where the required liquid velocity increases sub-linearly with current density. As an additional test, we also checked the dependence on electrode thickness by stacking two Ni felts together to give $L = 600$ μm. As predicted by Eq. (5) a lower liquid velocity is indeed required in this case.

The solid lines in Fig. 8 indicate Eq. (5) with a coefficient $c_2 = 5{\cdot}10^{-8}$ m^4/C/s, showing reasonable agreement for both $L = 300$ μm and 600 μm. With the parameters of Tables 1 and 2 this gives $s_0 \approx 0.97$, well within the range in which Eq. (5) was successfully verified against numerical simulations of Eq. (1).

We also performed similar experiments for configuration 2 of Fig. 5, showing that in this case a larger liquid velocity is required. The obtained value of $c_2 = 10^{-7}$ m^4/Cs corresponds with the values in Tables 1 and 2 with $s_0 \approx 0.98$. It seems likely that the hydrophilic nylon 1 with its relatively small aperture size of 35 μm of nylon 1, not too dissimilar from the pore sizes of the Ni felt shown in Fig. 4, avoids bubbles to enter the gap. Comparing with tests without a nylon spacer, an added advantage seems to be that bubbles trapped in the gap can be again removed upon increasing the flow rate. The aperture size of nylon 2 is however too large, both compared to the felt pore sizes as well as typical bubble sizes, to have a strong positive influence.

Finally, we also did an experiment with the Ni mesh in configuration 1. Here we found that for not too large current densities, bubbles in the gap could be largely avoided even without liquid flow. This shows that the hydrophilic nylon 1 for low current densities can act as a coarse separator for bubbles crossing over. Since electrolytically generated bubbles are typically of the order of 100 μm, this can be understood by the principle that such bubbles require additional surface deformation energy to cross into the gap.

4. Optimal design of membraneless flow-through electrolyzer

The experimental results from the previous section quantified what flow velocities allow operation without a real separator. Such a membraneless flow-through type of electrolyzer can operate with a significantly lower ohmic drop. However, thinner the gap, higher are the pumping losses. Therefore, a legitimate question is whether an overall benefit can be gained at all from using liquid flow and, if so, what the associated optimal parameters are. Using the experimental results of the previous section and simple well-established engineering relations, we will derive the parameters for such an optimal configuration. We define optimal here purely from the perspective of energy efficiency, leaving additional potential benefits in terms of hydrogen purity outside of our analysis.

Table 2
Approximate values used in the calculations, relevant for hydrogen evolution in configuration 1 with 30 w% KOH at ambient conditions. We calculate the effective electrode conductivity from $\kappa \approx \kappa_0 \epsilon^{1.5}$ with $\epsilon = 0.75$ and $\kappa_0 \approx 60$ S/m [69], the molar volume from $V_g = RT/p$, and the Tafel slope from $b = RT/\alpha F$ with charge transfer coefficient $\alpha = 1/2$,. The order of magnitude values in the second table were estimated from the measurements in sections 3.2 and 3.5. We additionally used $q = 3$.

μ_l	2	mPa s
μ_g	8.4	μPa s
K	40	S/m
B	50	mV
v_g	25	l/mol
Γ	73	mN/m
N	2	–
Ni-felt - conf. 1		
p_t	0.37	bar
K	10^{-13}	m^2
Λ	4/3	–
c_1	$5{\cdot}10^{-3}$	–
c_2	$5{\cdot}10^{-8}$	$\frac{\text{m}^4}{\text{Cs}}$
s_0	0.97	–

4.1. Cell model

We use a simple model for the cell voltage $E_{\text{cell}} = E_{oc} + \eta + jl/\kappa_0$ consisting of the open-circuit potential $E_{oc} = -\Delta G/F$, with ΔG the change in Gibbs free energy per mole of electrons involved, the activation overpotential η_0 at $x = 0$ given by Eq. (A.13) and ohmic drop over the gap jl/κ_0. Of the total power used per unit area per cross-sectional gap area $A = hw$, $E_{\text{cell}}j$, only $E_{oc}j$ can theoretically be recovered as electrical power in an ideal fuel cell, so we may define an energy efficiency as

$$\varphi \equiv \frac{jE_{oc}}{j(E_{oc} + \eta_0 + jl/\kappa_0) + P_{\text{pump}}/A}, \tag{6}$$

where P_{pump}/A is power used to pump the electrolyte, per unit electrode area A. We will assume that the total pressure drop

$$\Delta p = N\Delta p_{\text{gap}}, \quad \text{with } N \gg 1, \tag{7}$$

so that the pressure drop through the electrodes is much larger than that through the gap, so that the flow will distribute itself more or less homogeneously over the electrode surface. When the liquid, entering with a velocity $u_{in} = 2hu_l/l$, leaves homogeneously distributed along the height h of the electrodes under laminar conditions, the frictional pressure drop over the gap from bottom to top is $\Delta p_{\text{gap}} \approx 6\mu_l u_{in} h/l^2$ [71,72], or half the Hagen-Poiseuille pressure drop in case all the fluid would leave from the top.

The minimally required pumping power is given by the pressure drop times volumetric flow rate so that

$$\frac{P_{\text{pump}}}{A} = 2u_l\Delta p, \quad \Delta p = \frac{12N\mu_l u_l h^2}{l^3}. \tag{8}$$

Note that due to Eq. (7), in order to avoid flow maldistributions, the pressure drop is independent of electrode properties and depends only on properties of the gap.

4.2. Optimization

Equation. (5) shows that the minimum liquid velocity to avoid gas in the gap is minimized when $L \gg 2\kappa b/j$, in which case

$$u_l = j\sqrt{\frac{c_2 d_{\max}}{2\kappa b}}, \tag{9}$$

independent of the electrode and gap thicknesses L and l, respectively.

The pumping losses of Eq. (8) may be minimized by using as small as possible height h, which will however be limited by design practicalities. Alternatively, increasing the gap width l decreases the pumping losses, but increases the ohmic dissipation. The optimum is found by solving $\partial \varphi/\partial l = 0$ or $\frac{\partial}{\partial l}\left(\frac{j^2 l}{\kappa} + \frac{P_{\text{pump}}}{A}\right) = 0$ for l, which gives with Eqs. (8) and (9)

$$l_{\text{opt}} = (72\kappa\mu_l N)^{\frac{1}{4}}\sqrt{\frac{hu_l}{j}} = \left(\frac{36Nc_2\mu_l d_{\max} h^2}{b}\right)^{\frac{1}{4}}, \tag{10}$$

where $\frac{36Nc_2\mu_l}{b} = 48N\gamma\epsilon^3\frac{c_1}{\lambda}\frac{s_0^{q+1}}{(1-s_0)^{q-1}}\frac{\mu_g}{\mu_l}\frac{V_m}{nFb}$ [m]. The first result in Eq. (10) becomes that of Ref. [73] for a parallel plate electrolyzer, upon replacing $2Nh^2$ with l^2, reflecting the different flow outlet conditions. Using the values from Table 2, along with $\Delta p_{\text{el}}/\Delta p_{\text{gap}} = 10$ so that $N = 11$, and $h = 0.1$ m gives $l_{\text{opt}} \approx 0.5$ mm, similar to a typical commercial separator thickness [27,74], but with no solid material in the way giving a significantly lower ohmic resistance.

4.3. Pressure drop

Inserting Eq. (10) we find $\frac{j^2 l}{\kappa} + \frac{P_{\text{pump}}}{A} = \frac{4}{3}\frac{j^2 l}{\kappa}$ so that the pumping contribute to the total losses only 1/3-rd of the ohmic losses. With Eqs. (8)–(10)

$$\Delta p = \left(\frac{N\mu_l}{18\kappa^3}\right)^{\frac{1}{4}}\sqrt{\frac{hj^3}{u_l}} = \left(\frac{N\mu_l b}{c_2 d_{\max}}\right)^{\frac{1}{4}}\sqrt{\frac{h}{3\kappa}}j. \tag{11}$$

With $N = 11$, $h = 0.1$ m, $j = 0.3$ A/cm^2 and the properties from Table 1 and the Ni-felt of Table 1 this gives a modest pressure drop of $\Delta p_{\text{tot}} \approx 0.2$ bar. With $\Delta p = \Delta p_{\text{el}} + \Delta p_{\text{gap}}$ Eq. (7) implies that $\Delta p_{\text{el}} = \frac{N-1}{N}\Delta p$, which with Eq. (A.18) and Eq. (8) gives

$$K = \frac{l^3 L}{12(N-1)h^2}. \tag{12}$$

This criterion is required to give the electrodes sufficient hydraulic resistance to ensure a homogeneous flow distribution. With the previously obtained optimal value $l = 0.5$ mm, $N = 11$, $h = 0.1$ m, and say $L = 1$ mm, this gives $K = 10^{-13}$ m^2, equal to that of the Ni-felt of Tables 1 and 2

4.4. Mass transfer-limited

Finally, we consider the case where no gaseous products are evolved, but we instead want to use the flow to aid diffusive mass transfer in supplying reactants. In this case we replace Eq. (9) with $u_l = j/nFC$, the minimum liquid velocity required to supply enough reactants with inlet concentration C. To avoid back-flow of reaction products requires the Péclet number $\text{Pe} \equiv u_l L/D = jL/nFCD \gg 1$, with D the effective diffusivity of the product. This is often satisfied. Using the expression for the conductivity of a dilute electrolyte [59], we see that usually $2\kappa b \gtrsim nFCD$ when the concentration of the electrolyte exceeds that of the reactants. In this case we automatically have $\text{Pe} \gg 1$ when $jL/2\kappa b \gg 1$, a criterion preferable satisfied to minimize the activation overpotential of Eq. (A.13). Since the minimum velocity is independent of l we can use Eq. (10) to give

$$l_{\text{opt}} = (72\kappa\mu_l N)^{1/4}\sqrt{\frac{h}{nFC}}. \tag{13}$$

As an example we consider CO_2-reduction [24,42,75,76] to a non-gaseous product like formate. In a not too strong aqueous electrolyte, the CO_2 solubility at ambient pressure is around $C = 30$ mM, so that with $N = 11$, $\mu_l = 1$ mPas, $h = 0.1$ m, $n = 2$, and $\kappa = 10$ S/m we obtain $l_{\text{opt}} \approx 0.2$ mm, giving a conductance that is competitive with most anion exchange membranes [77].

Inserting Eq. (13) and $u_l = j/nFC$ in Eq. (8) gives $\Delta p \approx (N\mu_l/18\kappa^3)^{\frac{1}{4}}\sqrt{nFCh}j$. Using the same numbers as before, for a current density of 0.3 A/cm^2 we require a liquid velocity $u_l \approx 0.5$ mm/s, requiring roughly 0.6 bar of pressure drop.

5. Discussion

We have made various simplifications in the analysis that warrant further discussion. First of all, our assumption of a flow regime in which the gas forms a continuous phase rather than dispersed bubbles is likely valid for small enough pores, but the exact conditions under which Darcy's law holds are still under investigation [50]. For definiteness, we assumed power-law dependences on the liquid saturation of the relative permeabilities and capillary pressure in Eq. (1), but these can easily be replaced by different forms in the derivation of Eq. (5). Note that, since the derivation considers high liquid saturations, the model parameters are ideally obtained from empirical fits in this same range.

The free parameter s_0, representing the liquid saturation at the gap-electrode interface, is influenced by flow impacting bubble nucleation and release through drag and transport of dissolved reaction products. We found that s_0 could be reduced by adding a nylon spacer. The hydrophilic nature and relatively small aperture size likely gives it some of

the characteristics of a separator, albeit of much lower thickness and cost.

For simplicity, we did not include the impact of a spacer on the pressure drop in the gap. The factor N may be multiplied by a factor denoting deviation from the used Hagen-Poiseuille equation, and additionally divided by the pump efficiency. Given the very weak dependence of the optimal gap thickness of Eq. (10) on N, including these effects will only result in relatively small corrections. Spacers have been studied intensively for filtration and reverse osmosis applications, where improving mass transport is important. Increased mass transport also tends to lead to increased pressure drop, and typically a supra-linear dependence of pressure drop on velocity is observed due to inertial effects [78]. Spacers may be designed for low tortuosity by avoiding direction changes using, for example, primarily flow-aligned fibres.

We considered the porous anode and cathode to have similar properties and focussed on hydrogen evolution in application to water electrolysis. We note that the dynamic viscosity μ_g of oxygen is roughly twice that of hydrogen, but also $n = 4$ is double that for hydrogen evolution so that the relevant ratio μ_g/n in c_2 is similar.

Besides using smaller pores or thicker electrodes, a smaller electrode permeability K, if required by Eq. (12), may also be obtained by deploying an additional layer behind the electrodes with sufficient hydraulic resistance. The use of a smaller pore size however, counter-intuitively, has the advantage of reducing the overall pressure drop according to Eq. (11). The reason is of course that, by Eq. (5), smaller pores are predicted to require lower velocities to avoid bubbles entering the gap.

6. Conclusion

We studied here the potential of flow-through electrodes for membraneless operation in case of gas-evolving reactions. To minimize ohmic dissipation, a small gap between the electrodes is preferred, increasing pumping losses. Therefore, an important parameter is the minimally required flow velocity that allows effective membraneless operation without bubbles entering the gap. Previously studied bubble models cannot give insight into this parameter, nor are they suitable to describe electrodes with small pores. Small pores are preferred for their high reactive surface area and sufficient pressure drop to allow a homogeneous flow distribution. Therefore, we studied a multiphase Darcy-flow model from which we derived a simple analytical relation, Eq. (5), for the required liquid velocity. This relation was successfully verified with respect to numerical simulations and validated against experimental data.

A balance between ohmic and pumping losses lead to an explicit expression, Eq. (10), for the optimal gap thickness, showing that a significant reduction in resistance is possible compared to operation with a membrane. The optimal gap thickness depends most sensitively on the desired electrode height, dictated by practical design considerations, and only very weakly on material parameters of the electrolyte, electrode, and gap spacers.

We found that, up to modest current densities, a coarse Ni-mesh allowed operating without any liquid flow, when a finer simple nylon spacer was placed directly adjacent to the electrodes inside the gap. However, it seems likely that significant gas cross-over takes place in this case, while cross-over can be strongly reduced in the presence of liquid flow compared to operation with a membrane [27]. Also the use of coarse mesh electrodes, as in Refs. [14,15,79], requires relatively large flow velocities of many centimetres per seconds at higher current densities, and relatively large gap widths of a millimetre or more, even for small electrode dimensions of a few centimetres, to avoid flow maldistribution. We have shown that effective membrane-less operation with much smaller pores can be obtained at much smaller velocities, gap widths, with reasonable pressure drops. These flow velocities are nonetheless high enough to avoid mass transport limitations associated with dilute reactants and removal of products, strongly reducing the concentration polarization typically present in systems with a membrane, and potentially improving the product purity.

Declaration of competing interest

The authors declare that they have no known competing financial interests or personal relationships that could have appeared to influence the work reported in this paper.

Acknowledgements

We appreciate the help of Valerio Matrone and Jerry Westerweel with the visualization experiments. We acknowledge funding support from Shell Global Solutions International B.V., Netherlands, under agreement number PT73368.

Appendix A. Activation overpotential

Appendix A.1. General equations

The superficial gas velocity is given by Faraday's law as

$$u_g = \frac{V_m}{nF} i, \tag{A.1}$$

where i is the electronic current density, which varies from $i = 0$ at $x = 0$ to $i = j$ at $x = L$. Assuming the electrode conductivity is much higher than the electrolyte conductivity and assuming negligible concentration gradients of electrolyte and reactants, Ohm's law and the Tafel equation can be written as [80].

$$\frac{d\eta}{dx} = \frac{j - i}{\kappa s^m}, \tag{A.2}$$

$$\frac{di}{dx} = j_\star a e^{\eta/b}. \tag{A.3}$$

Here the surface overpotential η is equal to a constant minus the electrolyte potential, a is the active volumetric surface area, and b is the Tafel slope. We assumed the effective electrode conductivity can be written as κs^m with Archie's exponent m, often taken to be 1.5 or 2, to account for the presence of gas [81,82]. Equation A.3 gives the overpotential at $x = 0$ as

$$\eta_0 = b\ln\left(\frac{j}{aLj_\star \mathscr{E}}\right), \tag{A.4}$$

where the effectiveness factor $\mathscr{E} \equiv \frac{j}{Li'_0}$.

Appendix A.2. Bubble flow regime

For completeness and comparison we provide here the analysis for larger pore sizes in which a bubble flow regime may be assumed. The average interstitial gas and liquid velocities, v_g and v_l, are related to superficial velocities, u_g and u_l, as

$$v_g = \frac{u_g}{\epsilon(1-s)}, \quad v_l = \frac{u_l}{\epsilon s}. \tag{A.5}$$

Assuming the gas bubbles move with a fraction $f \equiv v_g/v_l$ of the liquid velocity, Eqs. (A.5) and (A.1) combine to give

$$s = \frac{1}{1+ri/j}, \quad r \equiv \frac{jV_m}{fu_l nF}, \tag{A.6}$$

with rf the ratio u_g/u_l at $x = L$. Taking a derivative of Eq. (A.3) with respect to x and inserting Eqs. (A.2) and (A.6) gives

$$\frac{d^2i}{dx^2} = \left(1+r\frac{i}{j}\right)^m \frac{j-i}{b\kappa}\frac{di}{dx}. \tag{A.7}$$

With $z \equiv \frac{di}{dx}$, we have $\frac{d^2i}{dx^2} = z\frac{dz}{di}$ so that Eq. (A.7), using Eq. (A.3), can be written as

$$\frac{d}{di}\left(j_\star a e^{\eta/b}\right) = \left(1+r\frac{i}{j}\right)^m \frac{j-i}{b\kappa}. \tag{A.8}$$

For constant parameters, we can integrate with respect to i between $i(0) = 0$ and $i(L) = j$ to give

$$e^{\eta_0/b} - e^{\eta_L/b} = \frac{j^2}{2j_\star ab\kappa_{\text{eff}}}, \tag{A.9}$$

where

$$\frac{\kappa}{\kappa_{\text{eff}}} = \frac{2}{r(1+m)}\left(\frac{(r+1)^{m+2}-1}{r(2+m)} - 1\right). \tag{A.10}$$

In the presence of bubbles, the effective conductivity κ_{eff} decreases below κ. With, for example $m = 1, 2$ or 3, Eq. (A.10) simplifies to

$$\frac{\kappa}{\kappa_{\text{eff}}} = 1 + r \times \begin{cases} \frac{1}{3} & m=1 \\ \frac{2}{3}+\frac{r}{6} & m=2 \\ 1+\frac{r}{2}+\frac{r^2}{10} & m=3. \end{cases} \tag{A.11}$$

For high current densities we can neglect the second term on the left-hand side of Eq. (A.9) with respect to the first, to obtain Eq. (A.4) with the electrochemical Thiele modulus $1/\mathscr{E}_{jL/\kappa_{\text{eff}}b\to\infty} = jL/2\kappa_{\text{eff}}b$. This is equal to the ohmic drop of ions reacting halfway the electrode at this effective conductivity [80,83,84]. Using the approximation of Ref. [80] we may write

$$\mathscr{E} \approx \frac{1}{1+jL/2\kappa_{\text{eff}}b}. \tag{A.12}$$

With this, a general expression

$$\eta_0 \approx b\ln\left(\frac{j}{j_\star aL} + \frac{j^2}{2b\kappa_{\text{eff}}j_\star a}\right), \tag{A.13}$$

is obtained. To explain the measured overpotentials of 0.1–0.5 V in Ref. [42] required unrealistically high gas fractions $\epsilon_g \geq 0.85$ associated with a very small slip factor $f = v_g/v_l \approx 0.0016$. Visual observations from our set-up of Fig. 6 rather showed $f \approx 1.8$ [70].

Appendix A.3. Darcy flow regime

As mentioned in the main text, numerical simulations with $s_0 \approx 1$ show that over most of the domain the two terms of Eq. (1) approximately balance so that

$$s \approx \frac{1}{1+\left(\frac{\mu_g u_g}{\mu_l u_l}\right)^{1/q}}. \tag{A.14}$$

Comparing with Eq. (A.6) we can redo the above analysis replacing ri/j with $R(i/j)^{1/q}$ in Eq. (A.8), where

$$R^q = \frac{\mu_g}{\mu_l}\frac{jV_m}{nFu_l} = \frac{\mu_g}{\mu_l}\frac{V_m}{nF}\sqrt{\frac{2\kappa b}{c_2 d_{\max}}}, \tag{A.15}$$

is the ratio between gas and liquid velocities at $x = L$ times the ratio μ_g/μ_l. In the second equality of Eq. (A.15) we inserted Eq. (9). Integrating Eq. (A.8) with $R(i/j)^{1/q}$ instead of ri/j gives, for example with $q = 3$

$$\frac{\kappa}{\kappa_{\text{eff}}} = 1 + R \times \begin{cases} \frac{9}{14} & m = 1 \\ \frac{9}{7} + \frac{9R}{20} & m = 2 \\ \frac{27}{14} + \frac{27R}{20} + \frac{R^2}{3} & m = 3. \end{cases} \tag{A.16}$$

With the values from Tables 1 and 2 for Ni-felt and, say, $C = 30$ mM, we obtain $R \approx 0.1$. From Eq. (A.16) this gives $\frac{\kappa}{\kappa_{\text{eff}}} \leq 1.2$ when $m \leq 3$, so only a small correction.

We conclude with providing an approximation for the pressure drop over the electrode in the presence of gas. Assuming $\mathscr{E} \approx 1$ we have $i \approx jx/L$ so that Eq. (3) gives $u_g \approx \frac{V_m j}{nF}\frac{x}{L}$. Using this in Eq. (A.14) and integrating the liquid phase pressure gradient, the second term in Eq. (1), gives with for example $q = 3$

$$\frac{K\Delta p_{\text{el}} L}{\mu_l u_l} \approx \int_0^L \left(1 + k\left(\frac{x}{L}\right)^{1/3}\right)^3 dx = 1 + \frac{9k}{4} + \frac{9k^2}{5} + \frac{k^3}{2}. \tag{A.17}$$

Here $k^3 = \frac{\mu_g}{\mu_l}\frac{V_m j}{nFu_l} = \frac{\mu_g}{\mu_l}\frac{V_m}{nF}\sqrt{\frac{jL}{c_2 d_{\max}}}$, where in the second equality we used Eq. (5) assuming $\mathscr{E} \approx 1$. So we see from Eq. (A.17) that, as long as $k \ll 1$, deviations from the single-phase pressure drop:

$$\Delta p_{\text{el}} = \frac{\mu_l u_l}{K} L \quad (k \ll 1), \tag{A.18}$$

will be small. With the values from Tables 1 and 2 for nickel felt, we obtain with $j = 0.5$ A/cm^2 a value $k \approx 0.1$, so that we can approximately neglect the effect of gas on the pressure drop.

References

[1] R. Sioda, K. Keating, in: aj Bard) (Ed.), Electroanalytical Chemistry 12 (1982).
[2] N. Hampson, "The electrochemistry of porous electrodes: flow-through and three-phase electrodes,".
[3] C. Oloman, Trickle bed electrochemical reactors, J. Electrochem. Soc. 126 (11) (1979) 1885–1892.
[4] C. Tennakoon, R. Bhardwaji, J. Bockris, Electrochemical treatment of human wastes in a packed bed reactor, J. Appl. Electrochem. 26 (1) (1996) 18–29.
[5] K. Kinoshita, S. Leach, Mass-transfer study of carbon felt, flow-through electrode, J. Electrochem. Soc. 129 (9) (1982) 1993–1997.
[6] X. Ke, J.M. Prahl, J.I.D. Alexander, J.S. Wainright, T.A. Zawodzinski, R.F. Savinell, Rechargeable redox flow batteries: flow fields, stacks and design considerations, Chem. Soc. Rev. 47 (23) (2018) 8721–8743.
[7] M.E. Suss, K. Conforti, L. Gilson, C.R. Buie, M.Z. Bazant, Membraneless flow battery leveraging flow-through heterogeneous porous media for improved power density and reduced crossover, RSC Adv. 6 (102) (2016) 100209–100213.
[8] J. Wang, H. Dewald, Deposition of metals at a flow-through reticulated vitreous carbon electrode coupled with on-line monitoring of the effluent, J. Electrochem. Soc. 130 (9) (1983) 1814–1818.
[9] J. Bisang, Theoretical and experimental studies of the effect of side reactions in copper deposition from dilute solutions on packed-bed electrodes, J. Appl. Electrochem. 26 (2) (1996) 135–142.
[10] A. Chu, M. Fleischmann, G. Hills, Packed bed electrodes. i. the electrochemical extraction of copper ions from dilute aqueous solutions, J. Appl. Electrochem. 4 (4) (1974) 323–330.
[11] C.S. Hofseth, T.W. Chapman, Electrochemical destruction of dilute cyanide by copper-catalyzed oxidation in a flow-through porous electrode, J. Electrochem. Soc. 146 (1) (1999) 199–207.
[12] S. Ho, Y. Wang, C. Wan, Electrolytic decomposition of cyanide effluent with an electrochemical reactor packed with stainless steel fiber, Water Res. 24 (11) (1990) 1317–1321.
[13] B. Ateya, E. Arafat, Applications of porous flow-through electrodes: I. an experimental study on the hydrogen evolution reaction on packed bed electrodes, J. Electrochem. Soc. 130 (2) (1983) 380.
[14] M.I. Gillespie, F. Van der Merwe, R.J. Kriek, Performance evaluation of a membraneless divergent electrode-flow-through (DEFT) alkaline electrolyser based on optimisation of electrolytic flow and electrode gap, J. Power Sources 293 (2015) 228–235.
[15] M.I. Gillespie, R. Kriek, Hydrogen production from a rectangular horizontal filter press divergent electrode-flow-through (DEFT) alkaline electrolysis stack, J. Power Sources 372 (2017) 252–259.
[16] M. Gillespie, R. Kriek, Scalable hydrogen production from a mono-circular filter press divergent electrode-flow-through alkaline electrolysis stack, J. Power Sources 397 (2018) 204–213.
[17] F. Yang, M.J. Kim, M. Brown, B.J. Wiley, Alkaline water electrolysis at 25 A/cm^2 with a microfibrous flow-through electrode, Adv. Energy Mater. (2020) 2001174.
[18] L. Arenas, C.P. de León, F. Walsh, Critical review–the versatile plane parallel electrode geometry: an illustrated review, J. Electrochem. Soc. 167 (2) (2020), 023504.
[19] J.A. Trainham, J. Newman, A comparison between flow-through and flow-by porous electrodes for redox energy storage, Electrochim. Acta 26 (4) (1981) 455–469.
[20] P.S. Fedkiw, Ohmic potential drop in flow-through and flow-by porous electrodes, J. Electrochem. Soc. 128 (4) (1981) 831–838.
[21] L. Joerissen, J. Garche, C. Fabjan, G. Tomazic, Possible use of vanadium redox-flow batteries for energy storage in small grids and stand-alone photovoltaic systems, J. Power Sources 127 (1–2) (2004) 98–104.
[22] P. Boissonneau, P. Byrne, An experimental investigation of bubble-induced free convection in a small electrochemical cell, J. Appl. Electrochem. 30 (7) (2000) 767–775.
[23] J.S. Hur, C.B. Shin, H. Kim, Y.S. Kwon, Modeling of the trajectories of the hydrogen bubbles in a fluorine production cell, J. Electrochem. Soc. 150 (3) (2003) D70–D78.
[24] Y. Chen, C. Xiang, N. Lewis, Modeling the performance of a flow-through gas diffusion electrode for electrochemical reduction of CO or CO_2, J. Electrochem. Soc. 167 (2020), 114503.
[25] P. Haug, M. Koj, T. Turek, Influence of process conditions on gas purity in alkaline water electrolysis, Int. J. Hydrogen Energy 42 (15) (2017) 9406–9418.
[26] P. Trinke, P. Haug, J. Brauns, B. Bensmann, R. Hanke-Rauschenbach, T. Turek, Hydrogen crossover in PEM and alkaline water electrolysis: mechanisms, direct comparison and mitigation strategies, J. Electrochem. Soc. 165 (7) (2018) F502–F513.
[27] J.W. Haverkort, H. Rajaei, Electro-osmotic flow and the limiting current in alkaline water electrolysis, J. Power Sources Adv. 6 (2020), 100034.
[28] J.T. Davis, J. Qi, X. Fan, J.C. Bui, D.V. Esposito, Floating membraneless pv-electrolyzer based on buoyancy-driven product separation, Int. J. Hydrogen Energy 43 (3) (2018) 1224–1238.
[29] S.M.H. Hashemi, P. Karnakov, P. Hadikhani, E. Chinello, S. Litvinov, C. Moser, P. Koumoutsakos, D. Psaltis, A versatile and membrane-less electrochemical reactor for the electrolysis of water and brine, Energy Environ. Sci. 2019 (5) (2019).

[30] B. El-Anadouli, M. Khader, M. Saleh, B. Ateya, Application of porous flow through electrodes: Iv. hydrogen evolution on packed bed electrodes of iron spheres in flowing alkaline solutions, J. Appl. Electrochem. 21 (2) (1991) 166–169.
[31] M.M. Saleh, Simulation of oxygen evolution reaction at porous anode from flowing electrolytes, J. Solid State Electrochem. 11 (6) (2007) 811–820.
[32] D.V. Esposito, Membraneless electrolyzers for low-cost hydrogen production in a renewable energy future, Joule 1 (4) (2017) 651–658.
[33] G.D. O'Neil, C.D. Christian, D.E. Brown, D.V. Esposito, Hydrogen production with a simple and scalable membraneless electrolyzer, J. Electrochem. Soc. 163 (11) (2016) F3012.
[34] R. Perskaya, I. Zaidenman, On liquid diffusion electrodes, in: Doklady Akademii Nauk, vol. 115, Russian Academy of Sciences, 1957, pp. 548–551.
[35] M. Paulin, D. Hutin, F. Coeuret, Theoretical and experimental study of flow-through porous electrodes, J. Electrochem. Soc. 124 (2) (1977) 180–188.
[36] M.M. Saleh, On the effectiveness factor of flow-through porous electrodes, J. Phys. Chem. B 108 (35) (2004) 13419–13426.
[37] M.M. Saleh, Mathematical modeling of gas evolving flow-through porous electrodes, Electrochim. Acta 45 (6) (1999) 959–967.
[38] B.G. Ateya, B.E. El-Anadouli, Effects of gas bubbles on the polarization behavior of porous flow through electrodes, J. Electrochem. Soc. 138 (5) (1991) 1331–1336.
[39] B. El-Anadouli, B. Ateya, Effects of gas bubbles on the current and potential profiles within porous flow-through electrodes, J. Appl. Electrochem. 22 (3) (1992) 277–284.
[40] M.M. Saleh, J.W. Weidner, B.G. Ateya, Electrowinning of non-noble metals with simultaneous hydrogen evolution at flow-through porous electrodes i. theoretical, J. Electrochem. Soc. 142 (12) (1995) 4113–4121.
[41] M. El-Deab, M. El-Shakre, B. El-Anadouli, B. Ateya, Electrolytic generation of hydrogen on Pt-loaded porous graphite electrodes from flowing alkaline solutions, J. Appl. Electrochem. 26 (11) (1996) 1133–1137.
[42] P. Bumroongsakulsawat, G. Kelsall, Tinned graphite felt cathodes for scale-up of electrochemical reduction of aqueous CO_2, Electrochim. Acta 159 (2015) 242–251.
[43] U. Pasaogullari, C.-Y. Wang, Two-phase transport and the role of micro-porous layer in polymer electrolyte fuel cells, Electrochim. Acta 49 (25) (2004) 4359–4369.
[44] A.Z. Weber, J. Newman, Effects of microporous layers in polymer electrolyte fuel cells, J. Electrochem. Soc. 152 (4) (2005) A677–A688.
[45] S. Litster, N. Djilali, Two-phase transport in porous gas diffusion electrodes, Dev. Heat Trans. 19 (2005) 175.
[46] B. Han, J. Mo, Z. Kang, G. Yang, W. Barnhill, F.-Y. Zhang, Modeling of two-phase transport in proton exchange membrane electrolyzer cells for hydrogen energy, Int. J. Hydrogen Energy 42 (7) (2017) 4478–4489.
[47] L. An, T. Zhao, Z. Chai, P. Tan, L. Zeng, Mathematical modeling of an anion-exchange membrane water electrolyzer for hydrogen production, Int. J. Hydrogen Energy 39 (35) (2014) 19869–19876.
[48] A. Zinser, G. Papakonstantinou, K. Sundmacher, Analysis of mass transport processes in the anodic porous transport layer in PEM water electrolysers, Int. J. Hydrogen Energy 44 (52) (2019) 28077–28087.
[49] A. Rajora, J.W. Haverkort, An analytical model for liquid and gas diffusion layers in electrolyzers and fuel cells, J. Electrochem. Soc. (2021). https://doi.org/10.1149/1945-7111/abe087.
[50] M. Ahmadlouydarab, Z.-S.S. Liu, J.J. Feng, Relative permeability for two-phase flow through corrugated tubes as model porous media, Int. J. Multiphas. Flow 47 (2012) 85–93.
[51] R. Alkire, B. Gracon, Flow-through porous electrodes, J. Electrochem. Soc. 122 (12) (1975) 1594.
[52] T. Risch, J. Newman, A theoretical comparison of flow-through and flow-by porous electrodes at the limiting current, J. Electrochem. Soc. 131 (11) (1984) 2551.
[53] F. Yang, M.J. Kim, B.J. Wiley, Alkaline water electrolysis at 20 A/cm^2 with a microfibrous, flow-through electrolyzer, in: Meeting Abstrcts, The Electrochemical Society, 2019, p. 1379, vol. MA2019–01.
[54] S. Shibata, The concentration of molecular hydrogen on the platinum cathode, Bull. Chem. Soc. Jpn. 36 (1) (1963) 53–57.
[55] H. Vogt, The concentration overpotential of gas evolving electrodes as a multiple problem of mass transfer, J. Electrochem. Soc. 137 (4) (1990) 1179.
[56] J.A. Leistra, P.J. Sides, Hyperpolarization at gas evolving electrodes–ii. Hall/heroult electrolysis, Electrochim. Acta 33 (12) (1988) 1761–1766.
[57] M.M. Bakker, D.A. Vermaas, Gas bubble removal in alkaline water electrolysis with utilization of pressure swings, Electrochim. Acta 319 (2019) 148–157.
[58] J.-Y. Moon, B.-J. Chung, Simulation of pool boiling regimes for a sphere using a hydrogen evolving system, Int. J. Heat Mass Tran. 151 (2020) 119441.
[59] J.W. Haverkort, Modelling and experiments of binary electrolytes in the presence of diffusion, migration, and electro-osmotic flow, Phys. Rev. Appl. 14 (2020), 044047. Published 26 October 2020.
[60] K. Nakornthap, R.D. Evans, et al., Temperature-dependent relative permeability and its effect on oil displacement by thermal methods, SPE Reservoir Eng. 1 (1986) 230–242, 03.
[61] A.E. Sáez, R. Carbonell, Hydrodynamic parameters for gas-liquid cocurrent flow in packed beds, AIChE J. 31 (1) (1985) 52–62.
[62] C.C. Huet, Semi-analytical Estimates of Permeability Obtained from Capillary Pressure, PhD thesis, Texas A&M University, 2006.
[63] M. Wyllie, M. Spangler, Application of electrical resistivity measurements to problem of fluid flow in porous media, AAPG (Am. Assoc. Pet. Geol.) Bull. 36 (2) (1952) 359–403.
[64] J. Tosoni, J.-C. Baudez, R. Girault, Effect of operating parameters on the dewatering performance of press filters: a sensitivity analysis, Dry. Technol. 33 (11) (2015) 1327–1338.
[65] A.D. Stickland, E.H. Irvin, S.J. Skinner, P.J. Scales, A. Hawkey, F. Kaswalder, Filter press performance for fast-filtering compressible suspensions, Chem. Eng. Technol. 39 (3) (2016) 409–416.
[66] R. Phillips, C.W. Dunnill, Zero gap alkaline electrolysis cell design for renewable energy storage as hydrogen gas, RSC Adv. 6 (102) (2016) 100643–100651.
[67] D. Eskin, Ultrasonic degassing of liquids, in: Power Ultrasonics, Elsevier, 2015, pp. 611–631.
[68] F. Hine, K. Murakami, Bubble effects on the solution IR drop in a vertical electrolyzer under free and forced convection, J. Electrochem. Soc. 127 (2) (1980) 292.
[69] D. Le Bideau, P. Mandin, M. Benbouzid, M. Kim, M. Sellier, Review of necessary thermophysical properties and their sensitivities with temperature and electrolyte mass fractions for alkaline water electrolysis multiphysics modelling, Int. J. Hydrogen Energy 44 (10) (2019) 4553–4569.
[70] V. Matrone, "Visualization and Analysis of Different Regimes in the Flow over a Porous Electrolytic Cell," Master's Thesis, Universita di Roma, Sapienza, 2019.
[71] A. Safaripour, F. Torabi, A. Nourbakhsh, Engineering model for coupling an electro–osmotic fuel micropump with a miniature direct methanol fuel cell, in: The 2nd Hydrogen & Fuel Cell (HFCC) Conference (2012), 2012.
[72] S.K. Karode, Laminar flow in channels with porous walls, revisited, J. Membr. Sci. 191 (1–2) (2001) 237–241.
[73] M.A. Modestino, D.F. Rivas, S.M.H. Hashemi, J.G. Gardeniers, D. Psaltis, The potential for microfluidics in electrochemical energy systems, Energy Environ. Sci. 9 (11) (2016) 3381–3391.
[74] M. Schalenbach, W. Lueke, D. Stolten, Hydrogen diffusivity and electrolyte permeability of the zirfon PERL separator for alkaline water electrolysis, J. Electrochem. Soc. 163 (14) (2016) F1480–F1488.
[75] V. Vedharathinam, Z. Qi, C. Horwood, B. Bourcier, M. Stadermann, J. Biener, M. Biener, Using a 3d porous flow-through electrode geometry for high-rate electrochemical reduction of CO_2 to CO in ionic liquid, ACS Catal. 9 (12) (2019) 10605–10611.
[76] N. Goos, Electrochemical Reduction of CO_2 to CO in a Flow-Through Electrolyser, Master thesis, Delft University of Technology, 2020.
[77] S. Gottesfeld, D.R. Dekel, M. Page, C. Bae, Y. Yan, P. Zelenay, Y.S. Kim, Anion exchange membrane fuel cells: current status and remaining challenges, J. Power Sources 375 (2018) 170–184.
[78] A. Da Costa, A. Fane, D. Wiley, Spacer characterization and pressure drop modelling in spacer-filled channels for ultrafiltration, J. Membr. Sci. 87 (1–2) (1994) 79–98.
[79] M. Gillespie, Design and Analysis of a Membraneless Divergent Electrode Flow through Electrolyser for Hydrogen Production, PhD Thesis, North-West University, 2018.
[80] J.W. Haverkort, A theoretical analysis of the optimal electrode thickness and porosity, Electrochim. Acta 295 (2019) 846–860.
[81] D. Bruggeman, The calculation of various physical constants of heterogeneous substances. i. the dielectric constants and conductivities of mixtures composed of isotropic substances, Ann. Phys. 416 (1935) 636–791.
[82] Y. Wang, S. Wang, S. Liu, H. Li, K. Zhu, Three-dimensional simulation of a pem fuel cell with experimentally measured through-plane gas effective diffusivity considering Knudsen diffusion and the liquid water effect in porous electrodes, Electrochim. Acta 318 (2019) 770–782.
[83] L. Austin, Tafel slopes for flooded diffusion electrodes, Trans. Faraday Soc. 60 (1964) 1319–1324.
[84] K. Scott, Short communication the effectiveness of particulate bed electrodes under activation control, Electrochim. Acta 27 (3) (1982) 447–451.